Eur. Phys. J. B (2016) 89: 57
DOI: 10.1140/epjb/e2016-60907-y

THE EUROPEAN PHYSICAL JOURNAL B

Regular Article

Quantum oscillations and wave packet revival in conical graphene structure

Debabrata Sinha[1,a] and Bertrand Berche[2]

[1] TIFR Centre for Interdisciplinary Sciences, 500075 Hyderabad, India
[2] Statistical Physics Group, Institut Jean Lamour, UMR CNRS No 7198, Université de Lorraine, B.P. 70239, 54506 Vandœuvre les Nancy, France

Received 23 November 2015 / Received in final form 19 January 2016
Published online 2 March 2016 – © EDP Sciences, Società Italiana di Fisica, Springer-Verlag 2016

Abstract. We present analytical expressions for the eigenstates and eigenvalues of electrons confined in a graphene monolayer in which the crystal symmetry is locally modified by replacing a hexagon by a pentagon, square or heptagon. The calculations are performed in the continuum limit approximation in the vicinity of the Dirac points, solving Dirac equation by freezing out the carrier radial motion. We include the effect of an external magnetic field and show the appearance of Aharonov-Bohm oscillations and find out the conditions of gapped and gapless states in the spectrum. We show that the gauge field due to a disclination lifts the orbital degeneracy originating from the existence of two valleys. The broken valley degeneracy has a clear signature on quantum oscillations and wave packet dynamics.

1 Introduction

The presence of topological defects in condensed matter systems can modify thoroughly their physical properties [1]. From the point of view of the geometrical effects, topological defects can induce curvature and/or torsion in the geometrical background. Differential geometry can thus be used for the study of a variety of physical systems, ranging from superfluid helium and its numerous spontaneous symmetry breakings [2], to liquid crystals [3] or mesoscopic physics [1,4]. The prominent work of Katanaev and Volovich [5] has shown the efficiency of this geometric approach to investigate the propagation of elastic waves in the presence of topological defects such as screw dislocations, edge dislocations or disclinations.

In a recent paper, one of us showed how the presence of a screw dislocation can generate spin current in an electron gas [4]. A screw dislocation is a source of torsion. Torsion can also be built in directly in the physical structure, like it is the case in chiral molecules where chirality couples to spin in the presence of spin-orbit interaction and can be used for spin selectivity applications, e.g. to polarize an electron beam [6] or to exalt the spin orientation of a spin current propagating through the molecule [7]. Edge dislocations are also the source of torsion, and their role was studied in topological insulators [8].

It is desirable to consider in this context topological defects that generate curvature. Single disclinations are line sources of curvature and they correspond to the generation of a conical geometry via the Volterra construction. Our aim in the present paper is to investigate the properties of a graphene layer in which the crystal symmetry is locally modified (a hexagon is for example substituted by a pentagon or a square (positive curvature), or by a heptagon (negative curvature)), giving rise to large scale properties analogous to thoses of the conical geometry mentioned above. The mechanisms of strain release leading to the formation of such defects in carbon nanotubes has been studied long ago [9]. The desire to employ graphene for studying curvature effects is motivated by the simplicity of the Hamiltonian and the important potential applications of graphene in nanoelectronics and possibly future quantum computing devices [10]. Carbon nanotubes are other famous elementary exemples of curvature effects in a carbon sheets [11], but the case of disclinations is different due to the presence of a singularity which sits at the defect location. Conical carbon nanostuctures can be produced experimentally e.g. by pyrolytic processes [12,13]. They commonly can reach the scale of several tens to several hundreds of nm.

Recently, there have been many studies on quantum rings, in which the confinement of electrons with phase coherence of wave function gives rise the Aharonov-Bohm [14] and Aharonov-Casher effects [15,16]. Quantum rings have been investigated both experimentally and theoretically in semiconductor devices [17] and also in graphene layers both in monolayers and bilayers [18–22]. In this context it is important to study the curvature effects on electron properties e.g. charge currents or quantum oscillations in a graphene monolayer ring. The eigenstates and eigenvalues of the ideal quantum ring are known in the absence of topological defect and our results should recover those of the literature[19–22] in that limit.

[a] e-mail: debabratas@tifrh.res.in

Graphene also offers a way to probe quantum field theory in condensed matter systems, as its low energy spectrum is described by the Dirac Hamiltonian of massless fermions. The Dirac electrons in graphene occur in two degenerate families which correspond to the presence of two different valleys in the band structure – a phenomenon known as *fermion doubling*. Due to the valley degeneracy, in many cases, it is difficult to observe the intrinsic physics of a single valley in experiments, because the two valleys have equal and opposite contributions to a measurable quantity. One way to break the valley degeneracy that we explore in the present paper is the production of pseudo-magnetic field in a single valley by a lattice defect. The field has an opposite sign in the other valley, so it lifts the degeneracy. The broken valley degeneracies leads to some interesting features on quantum oscillations and revival times of wave packets, which are the main concerns of this paper. We show that the signature of the broken valley degeneracy is clearly visible in the persistent current and the wave packet characteristic oscillation times.

Here, we consider a model of graphene with a wedge-dislocation, which can be understood from Volterra's cut-and-glue construction. The presence of the defect, although localized, stores an enormous amount of elastic energy which is released through the plastic bending of the backbone graphene sheet to form a cone (positive curvature) or a saddle (negative curvature). Such conical defects are elementary objects which are observed in graphene layers and in various carbon based structures [23–30]. Our calculations are based on the continuum model where pseudo-gauge fields due to the defects are coupled to the Dirac fermions [1,31]. After a general presentation, we will solve this model by freezing out the carriers'radial motion, keeping into account only their angular motion in a effectively one-dimensional system (namely a quantum ring). The more general 2d version of the problem will be briefly discussed, but it does not modify qualitatively our conclusions.

The paper is organized as follows: in Section 2 we present the theoretical model and numerical results for the energy spectrum, pseudo-spin polarization and charge current. In Section 3, the revivals and typical time scales of electrons wave function are presented. Section 4 contains a summary of the main results and conclusions.

2 Theory

In the low energy limit, the Hamiltonian of a graphene layer is given by

$$H = v_F(\tau_z\sigma_x p_x + \sigma_y p_y) + \Delta\tau_z\sigma_z \tag{1}$$

where $\vec{\sigma} = (\sigma_x, \sigma_y, \sigma_z)$, $\vec{\tau} = (\tau_x, \tau_y, \tau_z)$ are Pauli matrices denoting the sublattice and valley degrees of freedom, respectively, and v_F is the Fermi velocity. The finite mass term Δ, which might be caused by an interaction with the underlying substrate or by spin-orbit coupling is also taken into account [32,33]. The Hamiltonian (1) acts on the four-component spinors

$$\Psi(\vec{r}) = (\psi_{A+}(\vec{r})\ \psi_{B+}(\vec{r})\ \psi_{A-}(\vec{r})\ \psi_{B-}(\vec{r}))^T. \tag{2}$$

The pseudospin indices A and B label the two sublattices of graphene and the valley indices $+$ and $-$ refer to the two inequivalent Dirac points K and K' in the Brillouin zone. In a two dimensional plane for a flat graphene, the angular boundary condition for a Dirac spinor as it goes a closed path is given by

$$\Psi(r, \phi = 2\pi) = e^{i\pi\sigma_z\tau_z}\Psi(r, \phi = 0). \tag{3}$$

The presence of defects like disclination modifies the angular boundary conditions in equation (3). It is indeed known that deformations in the honeycomb lattice enter in the continuum limit description as pseudo-gauge fields coupled to the electron momentum as a vector potential [1,34,35]. We introduced a wedge disclination via the Volterra construction: first a sector of $n\pi/3$ is removed or added on the flat graphene lattice and this is then followed by gluing the edges of the cut (see Fig. 1). An index n defines the type of disclination in the honeycomb lattice. Keeping the symmetry of the lattice, a hexagon can now be replaced by a pentagon ($n = 1$), a square ($n = 2$), a heptagon ($n = -1$) or an octagon ($n = -2$) by the cut-and-glue procedure.

From equation (3), the wave function is multiplied by the factor $e^{i\phi\sigma_z\tau_z/2}$ to keep the Hamiltonian covariance. So, when a sector is removed/added from the graphene plane, the wave function should transform according to

$$\Psi(r, \theta = 2\pi) = -e^{i2\pi[1-(n/6)]\sigma_z\tau_z/2}\Psi(r, \theta = 0). \tag{4}$$

The additional minus sign in the boundary condition comes due to fact that the angular part of the wavefunction is taken as $e^{iJ\phi}$, where J is half odd integer (see Eq. (12)). When n is odd, an additional phase is required for the parallel transport of a Dirac fermion since when the spinor is transported around the apex, the phase mismatch due to the sublattice permutation (as for example a B site comes to a B site instead of A (see Fig. 1)) must be compensated to preserve the complete wave function single-valued. Considering all the factors, the angular boundary condition for a general n now becomes [24,36]

$$\Psi(r, \theta = 2\pi) = -e^{i2\pi[-\frac{n}{4}\sigma_y\tau_y + (1-(n/6))\frac{1}{2}\sigma_z\tau_z]}\Psi(r, \theta = 0). \tag{5}$$

Note that for even n, the matrix τ_y does not play any role, since for even n, $e^{i2\pi[-\frac{n}{4}\sigma_y\tau_y]} = \cos(\frac{\pm n\pi}{2})$. Equation (5) can be written as

$$\Psi(r, \theta = 2\pi) = \mathcal{P}_n\Psi(r, \theta = 0) \tag{6}$$

with

$$\mathcal{P}_n = e^{i\frac{n\pi}{3}(-\sigma_z\tau_z - 3\sigma_y\tau_y/2)}, \tag{7}$$

where we rescale the angle ϕ of the unfolded plane to the new angle $\theta = \phi/(1 - \frac{n}{6})$, where θ is varying from 0 to 2π. For more detail see the appendix. The general gauge transformation given in equation (6) for any type of disclination

$$\tilde{H}(r,\theta)=\begin{pmatrix}\tau\Delta & -i(\partial_r+\frac{1}{2r})-\frac{1}{r\Omega_n}(\partial_\theta+i\frac{\Phi}{\Phi_0}+i\frac{n}{4}\tau)\\ -i(\partial_r+\frac{1}{2r})+\frac{1}{r\Omega_n}(\partial_\theta+i\frac{\Phi}{\Phi_0}+i\frac{n}{4}\tau) & -\tau\Delta\end{pmatrix} \tag{11}$$

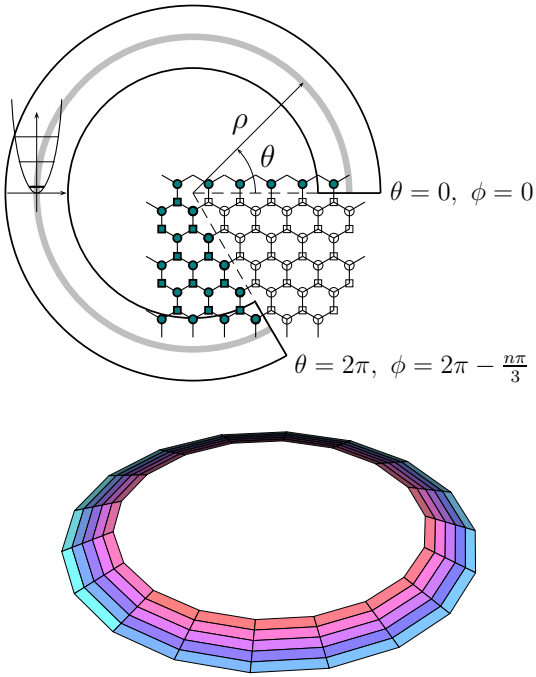

Fig. 1. Upper panel: unfolded plane of lattice where a wedge of angle $n\pi/3$ is removed ($n=1$ here). A potential (sketch on the left part of the ring) confines the electrons in the lowest radial mode on a ring of radius ρ, avoiding the singularity at the origin. We rescaled the angle ϕ of the unfolded plane to the new angle $\theta=\phi/(1-\frac{n}{6})$. The carbon atoms of the removed sector are denoted by open symbols, those which remain after the cut are represented in solid symbols. The defect, although localized, has a long distance effect. Here for example after gluing the edges of the removed sector, there remains a semi-infinite line of nearest neighbour atoms belonging to the same sublattice (circles in our case). A different perspective is shown in Figure 4 of reference [1]. Lower panel: the conical ring after the Volterra contruction.

is defined by the index $n=\pm1,\pm2$ defined above. For a local gauge transformation, equation (6) can be written as two singular gauge transformations

$$\Psi(r,\theta=2\pi)=U(\phi)V_n(\theta)\Psi(r,\theta=0), \tag{8}$$

where $U(\phi)=e^{-i\frac{\phi}{2}\sigma_z\tau_z}$ and $V_n(\theta)=e^{-i\frac{n\theta}{4}\tau_y\sigma_y}$.

Let us now consider an additional external magnetic flux Φ applied at the centre of the defect hole (a magnetic flux tube) corresponding to an azimuthal vector potential

$$\vec{A}=\frac{\Phi}{\Omega_n\Phi_0 r}\hat{\phi} \tag{9}$$

with $\Omega_n=(1-\frac{n}{6})$ and $\Phi_0=\frac{h}{e}$, the magnetic flux quantum. We write the Hamiltonian in equation (1) in polar coordinates and apply the gauge transformation through $U(\phi)$ and $V_n(\theta)$. The transformed Hamiltonian is denoted by $\tilde{H}(r,\theta)=U^\dagger V_n^\dagger H V_n U$,

$$\begin{aligned}\tilde{H}(r,\theta)=&\hbar v_F\left(k_r-\frac{i}{2r}\right)\tau_z\sigma_x\\&+\hbar v_F\left(k_\theta+\frac{\Phi}{\Omega_n\Phi_0 r}+\frac{n}{4\Omega_n r}\tau_z\right)\sigma_y+\Delta\tau_z\sigma_z\end{aligned} \tag{10}$$

where $k_r=-i\frac{\partial}{\partial r}$ and $k_\theta=-\frac{i}{r\Omega_n}\frac{\partial}{\partial\theta}$. Written in matrix form it is

see equation (11) above

where $\tau=+1$ and -1 correspond to the K and K' points, respectively. It is clear that the presence of the disclination leads to a rescaling of the angular coordinate in the Hamiltonian via the parameter Ω_n, but, more importantly, it breaks the symmetry between the two Dirac points as there is an explicit τ-dependent term which will lift the valley degeneracy.

The eigenstates of equation (11) are two component spinors which, for each valley index, are given in polar coordinates by

$$\Psi_\tau(r,\theta)=e^{iJ\theta}\begin{pmatrix}\Phi_A(r)\\ i\Phi_B(r)\end{pmatrix} \tag{12}$$

where J is the total angular momentum and $\Phi_A(r)$ and $\Phi_B(r)$ are linear combinations of Bessel functions due to the cylinder geometry. Now we will proceed the calculations by freezing the radial motion. Here we assume that the size of a defect is small as compared to the whole size of graphene monolayer and our interest is to study the defect influence on the physical properties of graphene. Considering a one-dimensional ring and simplifying the Schrödinger equation by discarding the radial variation of electron wavefunction is a correct approximation for a narrow ring for which the dynamics is frozen in the lowest radial mode. Excited radial modes have an energy much higher and can be neglected [37] when one studies low energy properties. The radial part of the momentum is thus set to zero ($P_\rho=-i\hbar(\frac{\partial}{\partial\rho}+\frac{1}{2\rho})\to 0$ in the sense of matrix elements [38,39]). In the case of a ring of fixed radius $r=\rho$, this leads to the substitution $\frac{\partial}{\partial r}\to-\frac{1}{2\rho}$ in equation (10) and the eigenstate (12) becomes

$$\Psi_\tau(r=\rho,\theta)=e^{iJ\theta}\begin{pmatrix}\Phi_A(\rho)\\ i\Phi_B(\rho)\end{pmatrix} \tag{13}$$

where $\Phi_A(\rho)$ and $\Phi_B(\rho)$ are now fixed amplitudes. Due to cylindrical symmetry, the spinors (13) are eigenfunctions of the total angular momentum $J_z=L_z+S_z$ with

$S_z = \frac{1}{2}\hbar\sigma_z$ and $\hbar(m+\frac{1}{2})$ is the eigenvalue of total angular momentum ($m \in \mathbb{Z}$). Note that we are considering here spinless electrons, hence the pseudo-spin contribution actually adds to orbital angular momentum. An additional term involving "real spin" should be taken into account if we were accounting for spin-orbit effects. People have often used different notations for the wave function [19,20,22] like

$$\Psi_\tau(\rho,\theta) = \begin{pmatrix} \Phi_A(\rho)e^{im\theta} \\ i\Phi_B(\rho)e^{i(m+1)\theta} \end{pmatrix}. \tag{14}$$

The wavefunction in equation (14) can be obtained from equation (13) by the unitary transformation $U = e^{-i\sigma_z\theta/2}$. So, the physical results should remain unchanged while using any of the two wavefunctions. In the following our calculations are always consistent in the limit $n = 0$ (no disclination) with the results obtained in references [19–22].

2.1 Eigenvalues and eigenfunctions

By writing now explicitly $\tilde{H}\Psi_\tau(\theta) = E\Psi_\tau(\theta)$, we obtain

$$\left[\frac{1}{\Omega_n}\left(J + \frac{\Phi}{\Phi_0} + \frac{n}{4}\tau\right)\right]\Phi_B = (\mathcal{E} - \tau\delta)\Phi_A \tag{15}$$

$$\left[\frac{1}{\Omega_n}\left(J + \frac{\Phi}{\Phi_0} + \frac{n}{4}\tau\right)\right]\Phi_A = (\mathcal{E} + \tau\delta)\Phi_B \tag{16}$$

with $\mathcal{E} = E/E_0$, where $E_0 = \frac{\hbar v_F}{\rho}$ and $\delta = \frac{\Delta}{E_0}$. The energy spectrum is given by solving equations (15) and (16)

$$\mathcal{E}^\tau_{n,J} = s\sqrt{\delta^2 + \frac{1}{\Omega_n^2}\left(J + \beta + \frac{n}{4}\tau\right)^2} \tag{17}$$

which may be also written as

$$\mathcal{E}^\tau_{n,J} = s\sqrt{\delta^2 + \frac{1}{\Omega_n^2}\left(m + \beta + 1 + \frac{n}{4}\tau\right)\left(m + \beta + \frac{n}{4}\tau\right) + \frac{1}{4\Omega_n^2}} \tag{18}$$

where we have defined the reduced magnetic flux $\beta = \frac{\Phi}{\Phi_0}$ and the labels $s = +1$ and $s = -1$ which refer to electron and hole bands respectively. As expected from our previous discussion, the energy spectra for K and K' valleys are not same. The valley degeneracy (τ) is broken by the presence of the disclination. This broken degeneracy has important effects on charge currents and wave packet revival time, which we will discuss later. The amplitudes, reminiscent of the radial part of two spinor components are

$$\Phi^\tau_A(\rho) = 1, \tag{19}$$

$$\Phi^\tau_B(\rho) = \frac{\nu_\tau}{\mathcal{E} + \tau\delta} \equiv \xi_\tau \tag{20}$$

where we defined, $\nu_\tau = \frac{J+\beta+\frac{n}{4}\tau}{\Omega_n}$.

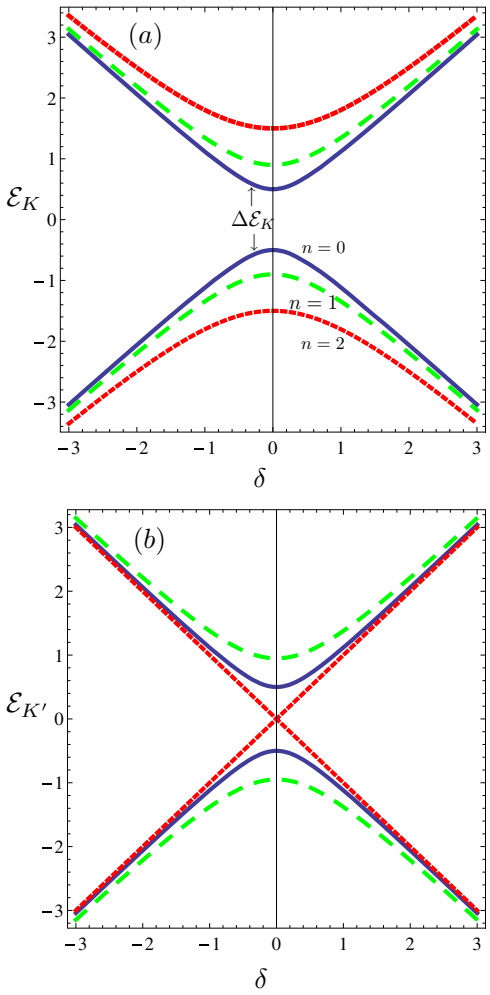

Fig. 2. Energy levels (a) $\mathcal{E}_K$ and (b) $\mathcal{E}_{K'}$ of a single layer graphene quantum ring as a function of a mass term δ with $\beta = 0$ and $m = 0$. Blue, green and red curves are for graphene with $n = 0, 1, 2$ respectively.

In the rest of the paper we fix the parameters $\Delta = 20$ meV [22] and $\rho = 50$ nm, except in Figure 2 where we vary reduced mass term δ by varying Δ for fixed ρ or vice versa. With a ring of width $w = 5$–10 nm, the typical gap between the ground state and the first excited radial mode is of order $\hbar v_F\pi/w \simeq 1$ eV (the typical wavevector scale due to lateral confinement is of order π/w), which justifies the 1d approximation used here. Figure 2 shows the energy level of a graphene ring for each valley as a function of the rescaled substrate interaction δ in absence of magnetic field (for reasons of clarity, in the legends of figures we will denote physical quantities with labels K or K' for the two Dirac points (like in $\mathcal{E}_K$) instead of the valley index τ). From equation (18), the energy difference between the valence and conduction bands is estimated to $\Delta\mathcal{E}^\tau_{n,J} = \frac{2}{\Omega_n}(J + \beta + \frac{n}{4}\tau)$ for the value of $\delta = 0$. So, the energy difference between two levels depends on the value of the disclination index n for a given value of quantum number J. It also takes different values at K and K' points. Interesting features can thus appear. For example,

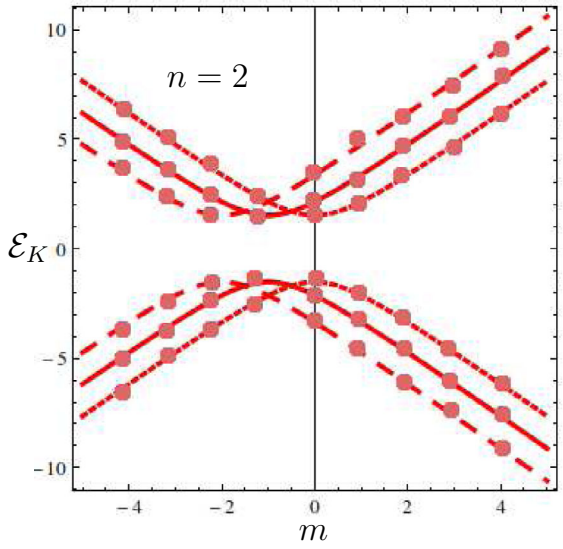

Fig. 3. Energy levels $\mathcal{E}_K$ for a graphene layer with a square defect as a function of m for different values of the reduced magnetic flux β. The solid curve is for $\beta = 0$, large dashed curve for $\beta = 1.0$ and small dashed curve for $\beta = -1.0$. The round symbols in the figure correspond to integer values of m.

at the K point, the graphene sheet with a square defect ($n = 2$) is gapped (insulator, with a gap of 39 meV while perfect graphene has a gap of 13.1 meV) but at the other Dirac point K' it is gapless (metallic) (see Fig. 2). It is gapped at both Dirac points for other values of n, but the values of the gaps differ at the two valleys. It is already known that a magnetic field can modify the gap (see e.g. experimental works in carbon nanotubes [40,41]), but here the dissymmetry between the two Dirac points is specific to the presence of the defect.

In presence of a finite value of magnetic flux, the system becomes gapless for a fixed value of $\beta = -(J+\frac{n}{4}\tau)$ i.e. $\Phi = -(m+\frac{1}{2}+\frac{n}{4}\tau)\Phi_0$ (for $\delta = 0$), otherwise the system remains gapped. For example, for $m = 0$ the graphene sheet with a pentagonal defect becomes gapless for $\Phi = -\frac{3}{4}\Phi_0$ and $\Phi = -\frac{1}{4}\Phi_0$ at K and K' points, respectively. Similarly, a graphene layer with a defect of index $n = 2$ becomes gapless for $\Phi = -\Phi_0$ and $\Phi = 0$ at K and K' points, respectively. Graphene with a negative curvature (n is negative) exhibits the opposite effect. As for example, graphene with $n = -1$ becomes gapless for $\Phi = -\frac{1}{4}\Phi_0$ and $\Phi = -\frac{3}{4}\Phi_0$ at K and K' points, respectively.

In Figure 3 we present the results for the energy levels as a function of the angular momentum m for $\beta = 0$, 1.0 and -1.0, respectively. From equation (18), the energy spectrum exhibits a minimum for $m = -(\frac{1}{2} + \beta + \frac{n}{4}\tau)$ for a given value of β and it is independent of δ. So, the gauge field due to curvature shifts the energy minimum and has an opposite effect at K and K' points. All these are consequences of the breaking of the valley degeneracy.

In Figures 4 and 5 we plot the energy as a function of the reduced magnetic flux (β) for different values of m.

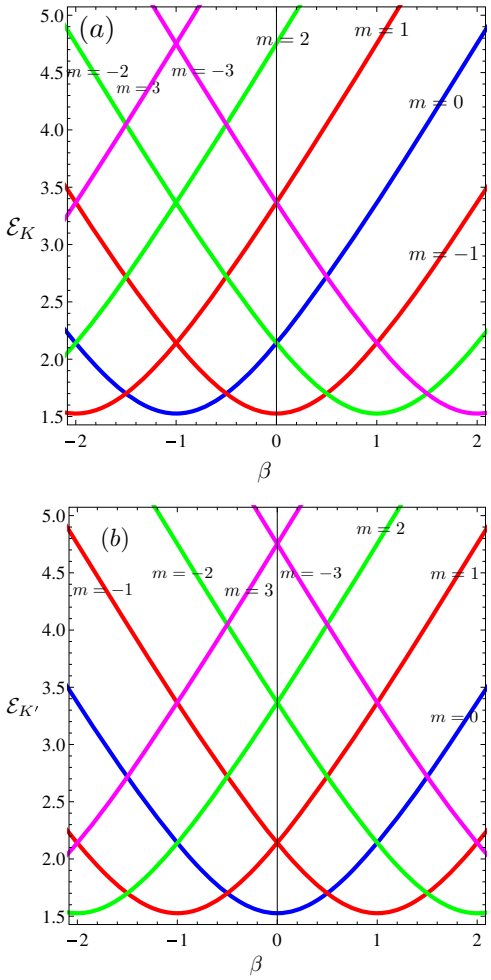

Fig. 4. Energy levels (a) $\mathcal{E}_K$ and (b) $\mathcal{E}_{K'}$ for a graphene layer with a square defect as a function of $\beta = \frac{\Phi}{\Phi_0}$. The blue curve is for $m = 0$, red for $m = -1$ and $m = 1$, green for $m = -2$ and $m = 2$, magenta for $m = -3$ and $m = 3$, respectively.

2.2 Pseudo-spin polarization

The pseudo-spin polarization is a contribution to the orbital angular momentum [42,43]. It can be calculated from the eigenvectors. The components of the pseudo-spin polarization are given by

$$\langle\sigma_x\rangle = 0 \tag{21}$$

$$\langle\sigma_y\rangle = \frac{2\xi_\tau}{1+{\xi_\tau}^2} \tag{22}$$

$$\langle\sigma_z\rangle = \frac{1-{\xi_\tau}^2}{1+{\xi_\tau}^2} \tag{23}$$

and are such that $\langle\sigma_x\rangle^2 + \langle\sigma_y\rangle^2 + \langle\sigma_z\rangle^2 = 1$. The result $\langle\sigma_x\rangle^2 = 0$ is due to the fact that $\sigma_x\tilde{H}\sigma_x = -\tilde{H}$, hence $E\langle\sigma_x\rangle = -E\langle\sigma_x\rangle$ for eigenstates of energy E. A physical reason for this symmetry is connected to the narrow ring approximation which constraints the average of terms containing σ_x to vanish in equation (10). Using equations (21) and (22) it is easy to calculate the pseudo-spin polarization in polar co-ordinates σ_ρ and σ_θ.

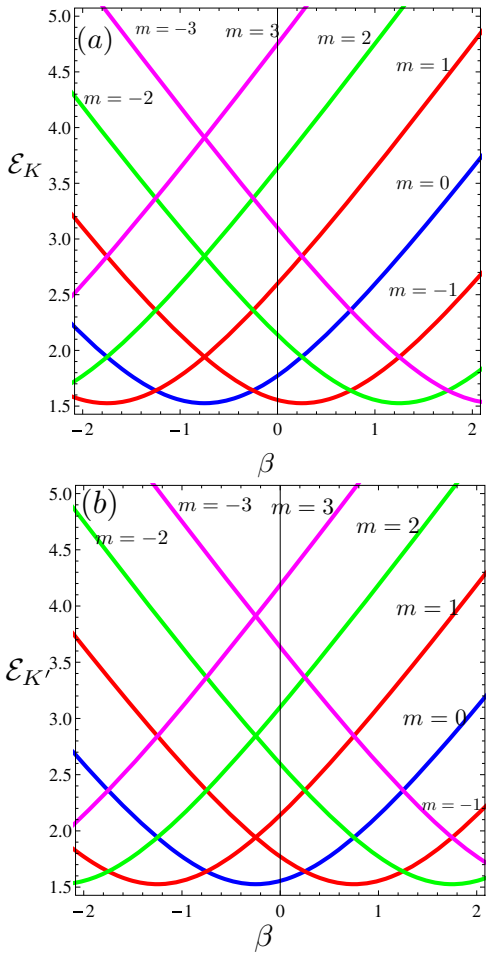

Fig. 5. Energy levels (a) $\mathcal{E}_K$ and (b) $\mathcal{E}_{K'}$ for a pentagonal defect in a graphene layer as a function of $\beta = \frac{\Phi}{\Phi_0}$. The color significance is the same as in Figure 4.

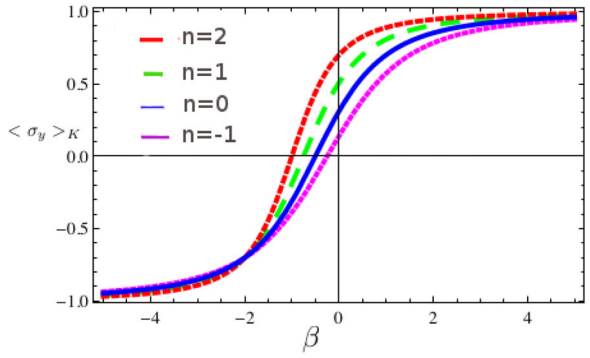

Fig. 6. Pseudo-spin polarization $\langle\sigma_y\rangle$ as a function of β for $m = 0$ at point K. The red, green, blue and magenta curve are for graphene with $n = 2, 1, 0, -1$, respectively.

In Figure 6 we show the curvature effect on pseudo-spin polarization (σ_y) of a disclinated graphene. It is seen that at $\beta = 0$, positive curvature has a larger spin-polarization. The blue curve in Figure 6 is for a monolayer graphene ring. Due to the ring geometry it also has a permanent pseudo-spin polarization at $\beta = 0$.

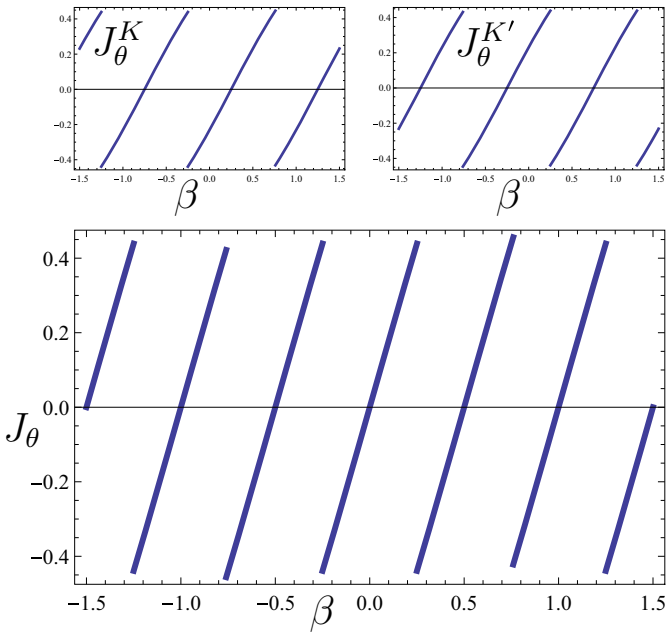

Fig. 7. Charge current J_θ for a pentagon graphene ring. Upper panels show the charge current for the valleys $\tau = +1$ (left) and $\tau = -1$ (right). Main panel is for the total charge current with the frequency doubling. The oscillations are manifestations of the Aharonov-Bohm effect.

2.3 Charge currents

The angular velocity is defined according to $v_\theta = \frac{i\rho}{\hbar}[\tilde{H}(\rho,\theta),\theta] = \frac{1}{\Omega_n}\sigma_y$. So, the current is given by

$$J_\theta = \frac{1}{\Omega_n}(\Phi_A^{\tau\star}\Phi_B^\tau + \Phi_A^\tau\Phi_B^{\tau\star}) = \frac{2}{\Omega_n}\xi_\tau. \tag{24}$$

The expressions of the angular current in valleys K and K' are found to be

$$J_\theta^K = \frac{2}{\Omega_n^2}\frac{(J+\beta+\frac{n}{4})}{\mathcal{E}_K+\delta}, \tag{25}$$

and

$$J_\theta^{K'} = \frac{2}{\Omega_n^2}\frac{(J+\beta-\frac{n}{4})}{\mathcal{E}_{K'}-\delta}. \tag{26}$$

We observe that there are three contributions, first a term due to the orbital angular momentum (J), second a term due to the presence of the magnetic flux (β) and finally the defect contribution (n). It is worth mentioning that the defect contributions are opposite in the two valleys. The total current is now

$$\begin{aligned} J_\theta &= J_\theta^K + J_\theta^{K'} \\ &= \frac{2}{\Omega_n^2}\frac{(J+\beta)(\mathcal{E}_K+\mathcal{E}_{K'}) - \frac{n}{4}[(\mathcal{E}_K-\mathcal{E}_{K'})-2\delta]}{(\mathcal{E}_K+\delta)(\mathcal{E}_{K'}-\delta)}. \end{aligned} \tag{27}$$

In Figures 7 and 8 we have shown the charge current of a graphene layer with positive curvature defects of indices $n = 1$ and $n = 2$. Note that the current contributions

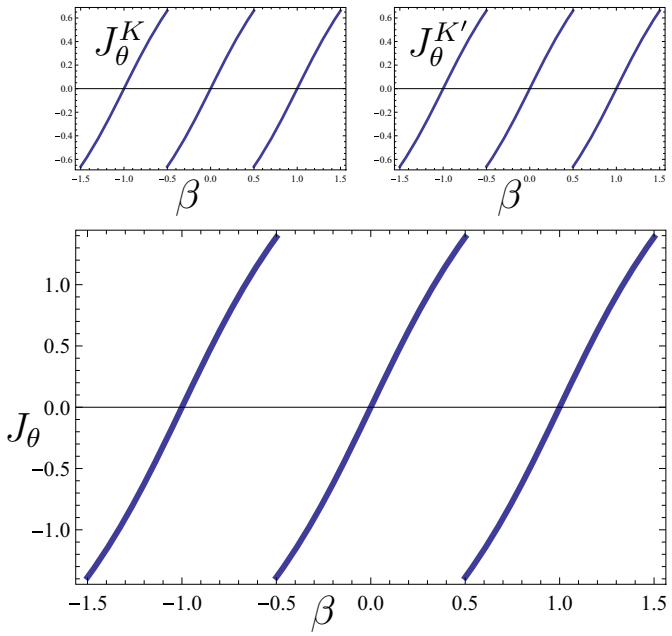

Fig. 8. Charge current J_θ for a graphene ring with square defect for $\tau = +1$ and $\tau = -1$ in the upper panels. The total charge current is shown in the main panel. It essentially has the same features as a single-valley contribution.

from K and K' are not the same in the case of pentagon graphene. This is also true generally for odd n and the total current consequently exhibits an oscillation with the field which has half the periodicity of that of single-valley current. For even n, the contribution from the K-valley and K' are the same and they oscillate in phase, this is also true for $n = 0$ [20]. The magnetic flux periodicity of the total charge current thus depends on the parity of the index n.

3 Revival and classical periodicity

The revival phenomenon has attracted broad interest over the past decade. Revivals, and associated fractional revivals, are investigated theoretically and also observed experimentally in Rydberg wave packets in atoms, molecules, molecular vibrate states and Bose-Einstein condensates [44–47]. The revival method is used to control the wave packet [48–50], or for isotope separation [51–53] to give examples of applications. Revivals happen when the wave packet comes back to its initial shape during its temporal evolution. The time at which the revival occurs is called revival time ($T_{\rm R}$). The periodicity of the wave packet revivals depends on the energy eigenvalue spectrum and is independent of the initial shape of the wave function. For an initial wave packet, written as a superposition of eigenstates sharply peaked around some level m_0 (e.g. the quantum label J of Sect. 2), the Taylor expansion of the energy spectrum E_m around the the energy E_{m_0}, is given by

$$E_m \simeq E_{m_0} + E'_{m_0}(m - m_0) + \frac{E''_{m_0}}{2}(m - m_0)^2 + \dots \quad (28)$$

where every coefficient of the Taylor expansion in equation (28) gives an important characteristic time scale for the propagating wave packet [54,55]. The temporal evolution of the localized bound state χ for a time independent Hamiltonian can be written in terms of the eigenfunctions u_m and eigenvalues E_m as

$$\chi = \sum_{m=0}^{\infty} a_m u_m e^{-iE_m t/\hbar} \quad (29)$$

with $a_m = \langle u_m | \chi \rangle$. If the coefficient a_m are considered to be tightly spread around a large $m_0 \gg |m - m_0|$ and $m_0 \gg 1$, and taking into account equation (28), one has

$$e^{-iE_m t/\hbar} = e^{-i\omega_0 t - 2\pi i(m-m_0)t/T_{\rm Cl} - 2\pi i(m-m_0)^2 t/T_{\rm R} + \dots} \quad (30)$$

which defines different time scales, that is, $T_{\rm R} = 4\pi\hbar/|E''_{m_0}|$ and $T_{\rm Cl} = 2\pi\hbar/E'_{m_0}$. The propagating wave initially evolves quasiclassically and oscillates with a period $T_{\rm Cl}$, then it will spread and collapse (delocalize). At later times, given by integral multiples of $T_{\rm R}/2$, the wave packet will regain its initial shape and oscillate again with a period $T_{\rm Cl}$. Moreover, at times that are rational fractions of $T_{\rm R}$, the wave packet splits into a collection of scaled and reshifted copies called fractional revivals. A longer time scale can be defined beyond $T_{\rm R}$, the so called super-revival time, at which a new cycle of full and fractional revivals emerges again [56].

We shall construct the initial wavepacket as a linear combination

$$\chi_0(\rho, \theta) = \sum_m c_m \Psi_m(\rho, \theta) \quad (31)$$

centered around a given eigenvalue E_{m_0}, with Gaussian distributed coefficients $c_m = \sqrt{\frac{1}{\sqrt{\pi}\sigma}} e^{-\frac{(m-m_0)^2}{2\sigma^2}}$, where σ is the variance of the distribution. We can write the temporal evolution of the initial wavepacket as:

$$\chi_t(\rho, \theta) = \sum_m c_m \Psi_m(\rho, \theta) e^{-iE_m t/\hbar}. \quad (32)$$

The study of the time dependence of the wavepacket is calculated in terms of the autocorrelation function, that is, the overlap of the initial state χ_0 in equation (31) and its temporal evolution in equation (32):

$$A(t) = \langle \chi_0 | \chi_t \rangle = \int_0^{2\pi} \chi_0^*(\rho, \theta) \chi_t(\rho, \theta) d\theta. \quad (33)$$

If we consider the expansion of equation (28), $A(t)$ can be written as

$$A(t) = \sum_m |c_m|^2 e^{-iE_m t/\hbar}. \quad (34)$$

The occurrence of revivals corresponds to a complete overlap with the initial state, for which $|A(t)|^2$ returns to its initial value of unity. In this case the classical period and

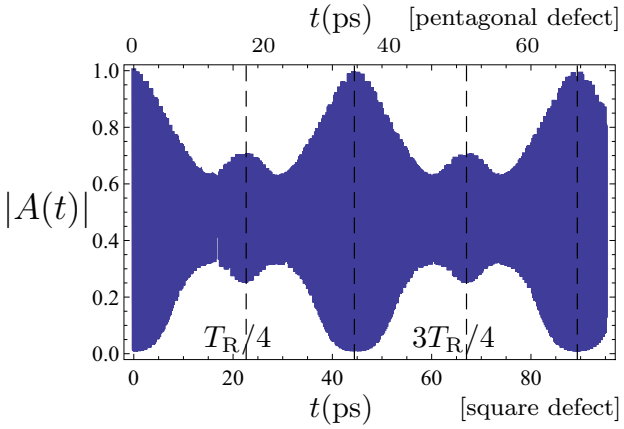

Fig. 9. Time dependence of $|A(t)|$ for initial wavepacket with $m = 5$ and $\sigma = 1.5$ at the K point. Upper horizontal axis: $T_{\rm R} = 65.56$ ps with pentagonal defect. Lower horizontal axis: $T_{\rm R} = 89.35$ ps with a square defect. The difference lies in the time scales (horizontal axis).

Table 1. Classical and Revival times at the two isotropic valleys K and K' for a graphene quantum ring with index $n = 1$ and $n = 2$ with $\rho = 50$ nm and $\Delta = 20$ meV. The initial wavepacket were built as a superposition of Gaussian-distributed state of width $\sigma = 1.5$.

m	$T_{\rm Cl}(K)$ $n=1$	$T_{\rm Cl}(K')$, $n=1$	$T_{\rm Cl}(K)$ $n=2$	$T_{\rm Cl}(K')$ $n=2$
5	0.2668 ps	0.2681 ps	0.2133 ps	0.2146 ps
10	0.2624 ps	0.2626 ps	0.2112 ps	0.2114 ps
15	0.2614 ps	0.2615 ps	0.2108 ps	0.2108 ps
20	0.2611 ps	0.2611 ps	0.2106 ps	0.2106 ps
m	$T_{\rm R}(K)$ $n=1$	$T_{\rm R}(K')$, $n=1$	$T_{\rm R}(K)$ $n=2$	$T_{\rm R}(K')$ $n=2$
5	65.56 ps	50.68 ps	89.35 ps	53.20 ps
10	407 ps	354 ps	539 ps	406.71 ps
15	1268 ps	1152 ps	1650 ps	1360.94 ps
20	2888 ps	2685 ps	3721 ps	3216.25 ps

the revival time can be calculated from equations (28) and (18)

$$T_{\rm Cl} = \frac{2\pi\rho\Omega_n}{v_F}\sqrt{1+\frac{\delta^2\Omega_n^2}{(m+\frac{1}{2}+\frac{n}{4}\tau)^2}} \qquad (35)$$

and

$$T_{\rm R} = \frac{4\pi\rho\Omega_n^2}{v_F}\frac{[\delta^2+\frac{1}{\Omega_n^2}(m+\frac{1}{2}+\frac{n}{4}\tau)^2]^{\frac{3}{2}}}{\delta^2} \qquad (36)$$

for $\beta = 0$. The characteristic times are depending on the type of disclination and are different at K and K' points. In Figure 9 we show plots of the time dependence of $|A(t)|$ for pentagonal and square defects in graphene. In all case we choose $\rho = 50$ nm, $\Delta = 50$ meV and $m_0 = 5$. For pentagonal graphene the initial wavepacket has a fast quasiclassical oscillatory behavior with a period $T_{\rm Cl} = 0.2668$ ps; this quasiclassical amplitude decreases and later there is regeneration of the quasiclassical behaviour at half the revival time $T_{\rm R}/2 = 32.78$ ps. Similarly, for a square defect $T_{\rm Cl} = 0.2133$ ps and $T_{\rm R} = 89.35$ ps (see Tab. 1).

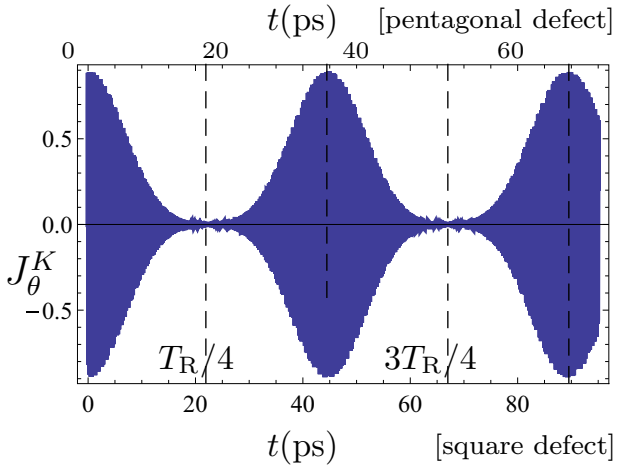

Fig. 10. Time evolution of $J_\theta^K(t)$ for a pentagonal defect (upper horizontal axis) and a square defect (lower horizontal axis). The difference between the two cases lies in the time scales.

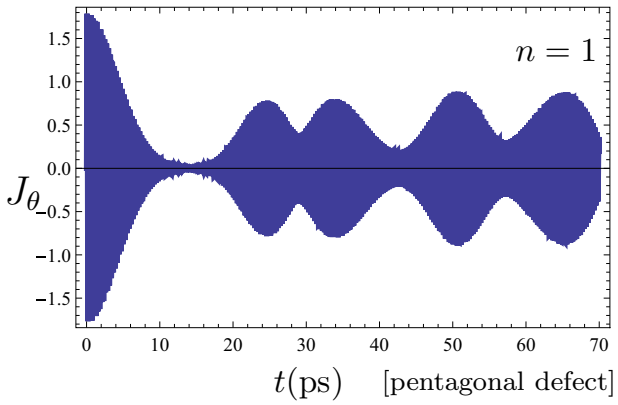

Fig. 11. Time evolution of total angular current J_θ for a pentagon defect.

It is also seen from the results listed in Table 1 that the classical and revival times are different at K and K' (see Fig. 10 at K point). This difference in time scales actually destroys the oscillating behaviour of the total charge current as shown in Figure 11 for a pentagonal defect in graphene. This unusual behaviour is one of the main results of this paper.

To investigate the time evolution of angular current J_θ in equation (27), we expand in the base of $\Psi_m(\rho,\theta)$. One finds for the expected temporal evolution of the current [57]

$$J_\theta^K(t) = v_F\sum_{m=1}^{\infty}|c_{m,m-1}|^2\sin[(E_m - E_{m-1})t/\hbar]. \qquad (37)$$

One can find $E_m - E_{m-1} \simeq E'_{m_0} + E''_{m_0}(m-m_0)$ from which the scales $T_{\rm Cl}$ and $T_{\rm R}$ arise. We show in Figure 10 the time behaviour of the current J_θ for defects of indices $n = 1$ and $n = 2$. After a few periods the initial wave packet enters the collapse phase and the quasiclassical oscillatory behaviour of the currents vanishes, only to re-emerge later at half the revival time.

Our results are also valid in 2d. In 2d the radial part of the bound states is given in terms of modified Bessel functions which decay exponentially for $r \to \infty$. The energy spectrum is obtained from the transcendental equation that arises after imposing infinite-mass boundary conditions, given by $\Phi_B(r,\theta)/\Phi_A(r,\theta) = i\tau(\hat{n}\cdot\hat{r})e^{i\tau\theta}$, where the normal to the boundaries is $\hat{n} = \pm\hat{r}$ for the inner $(-)$ and outer $(+)$ of a ring centering of a disclination [18,31]. Using the asymptotic form of the modified Bessel function and with the assumption that the ring radius is much larger than its width, the eigenvalues are given by [18],

$$E^{\tau}_{k,J} = \pm\epsilon_k \pm \lambda_k\nu_\tau\left(\nu_\tau \mp \frac{\tau}{(k+\frac{1}{2}\pi)}\right) \tag{38}$$

where $\epsilon_k = \hbar v_F(k+\frac{1}{2})\pi/w$ with $k = 0, 1, 2\ldots$ which refer to the radial quantum labels and $\lambda_k = (\frac{\hbar v_F}{a})^2/2\epsilon_k$. w is the width of the ring. The angular quantum number J appears through the ν_τ coefficients introduced in Section 2. In equation (38), it is clear that $E^+ \neq E^-$ even for $\beta = 0$ i.e the valley degeneracy is broken and our main results obtained in the limit of an infinitely narrow ring still hold.

4 Summary and conclusions

In this paper, we have shown how a specific type of topological defect, a disclination which is a source of curvature and produces an effective gauge field coupled to the graphene electrons can modify the physical properties of the material by the breaking of valley degeneracies.

- The presence of the disclination (the effect of which is measured by a non-vanishing integer index n which quantifies the curvature induced) modifies the energy spectrum (which in particular can be gapless at one Dirac point and gapped at the other) and has the effect of shifting the magnetic flux in opposite directions at the two Dirac points K and K'.
- As a consequence, there is a modification of the charge current, and the pseudo-magnetic field produced by the disclination having opposite signs at the two Dirac points, the currents there partially cancel each other. The total current has a half periodicity for odd values of the curvature index n. Although for even n this scenario is different, contribution from two Dirac points are in same phase and enhance the total charge currents.
- The disclination may also enhance or smoothen (depending on the sign of n, hence, of positive or negative curvature) the pseudo-spin polarization which is a contribution to the orbital angular momentum.
- This also leads to remarkable features on quantum oscillations and revival times of wave packets, for example the fact that the revival times are not exactly identical at the two Dirac points. As a consequence, the oscillating behavior of the current is partially destroyed with time. This is true for any type of disclinations in graphene.

There should exist experimental signatures of these features. For example in the presence of a single square disclination, the graphene sheet is gapped at K-point but gapless at K' and thus the conductivity of the metallic state should be half that of the pure graphene sheet. The change of periodicity in the current dependence on the magnetic flux is even a more obvious signature. The model studied here has some limitations. In graphene, the defects often appear in pairs (Stone-Wales defect) or form close to grain boundaries to minimize energy, but as mentioned in the introduction, nanocones can be produced for which the formalism used here applies.

Author contribution statement

Both authors contributed equally to the manuscript.

We thank Ernesto Medina for useful correspondence. D.S. likes to thank the Statistical Physics Group in the University the Lorraine, where part of this work has been done, for hospitality.

Appendix

In a continuum model, the Hamiltonian of graphene with a Haldane mass term is given by

$$H = v_F(\tau_z\sigma_x p_x + \sigma_y p_y) + \Delta\tau_z\sigma_z. \tag{A.1}$$

The total wavefunction for this Hamiltonian is

$$\begin{aligned}\psi_{tot}(\vec{r}) = \psi_{A+}(\vec{r})u_{A+}(\vec{r}) + \psi_{B+}(\vec{r})u_{B+}(\vec{r})\\ +\psi_{A-}(\vec{r})u_{A-}(\vec{r}) + \psi_{B-}(\vec{r})u_{B-}(\vec{r})\end{aligned} \tag{A.2}$$

where A and B are the two sublattices of graphene and $+$ and $-$ refer to the two inequivalent Dirac points K and K' in the Brillouin zone. The base function are denoted by $u_{A+/B+}$ and $u_{A-/B-}$ at the valleys K and K'. The envelope function is four component spinor,

$$\Psi(\vec{r}) = [\psi_{A+}(\vec{r}), \psi_{B+}(\vec{r}), \psi_{A-}(\vec{r}), \psi_{B-}(\vec{r})]^T. \tag{A.3}$$

The complex phases on site A/B are given by the Bloch factor $e^{\pm i\vec{r}.\vec{K}}$. We use the notation $\eta = e^{i2\pi/3}$ and $\bar{\eta} = e^{-i2\pi/3}$ in Figure A.1. for the distribution of the phase in the basis functions. Now matching the phase of the basis functions for even n, the boundary condition for the envelope function are:

$$\begin{aligned}\Psi(r,\phi = 4\pi/3) = e^{i\frac{2\pi}{3}\sigma_z\tau_z}\Psi(r,\phi=0), n = +2\\ \Psi(r,\phi = 8\pi/3) = e^{-i\frac{2\pi}{3}\sigma_z\tau_z}\Psi(r,\phi=0), n = -2.\end{aligned} \tag{A.4}$$

For odd value of n, the sublattice symmetry is broken. We can find boundary conditions by matching the phase from opposite sublattice components in opposite valleys. As for example for 60° (i.e. for $n = +1$) the boundary conditions is given by (see Ref. [31])

$$\Psi\left(\phi = \frac{5\pi}{3}\right) = \begin{pmatrix} 0 & 0 & 0 & \eta \\ 0 & 0 & \bar{\eta} & 0 \\ 0 & \bar{\eta} & 0 & 0 \\ \eta & 0 & 0 & 0 \end{pmatrix}\Psi(\phi = 0) \tag{A.5}$$

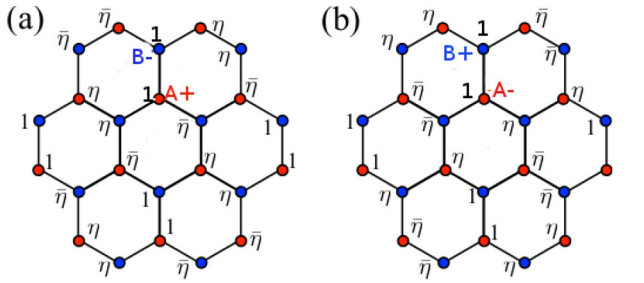

Fig. A.1. The complex phase of the base in graphene. $A+$ and $B+$ are sublattice components at the valley K where $A-$ and $B-$ are sublattice components at the valley K'; (a) corresponds to the base functions u_{A+} and u_{B-}; (b) corresponds to the base functions u_{A-} and u_{B+}.

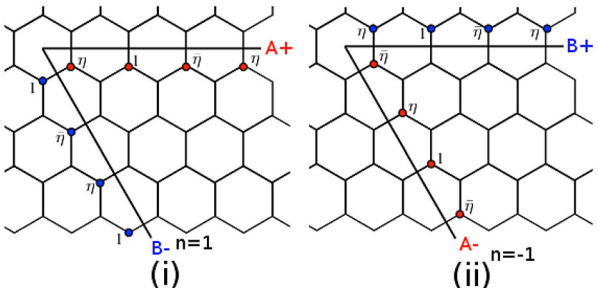

Fig. A.2. (i) and (ii) correspond to the complex phases for $+60°(n = 1)$ and $-60°(n = -1)$.

and for $-60°$ (i.e. for $n = -1$) as follows

$$\Psi\left(\phi = \frac{7\pi}{3}\right) = \begin{pmatrix} 0 & 0 & 0 & \bar{\eta} \\ 0 & 0 & \eta & 0 \\ 0 & \eta & 0 & 0 \\ \bar{\eta} & 0 & 0 & 0 \end{pmatrix} \Psi(\phi = 0) \tag{A.6}$$

with the rescaled variable $\theta = \phi/\Omega_n$ (with $\Omega_n = 1 - n/6$), equations (A.4)–(A.6) can be written in compact form

$$\Psi(\theta = 2\pi) = e^{-i\frac{n\pi}{3}\left(\frac{\sigma_z\tau_z + 3\sigma_y\tau_y}{2}\right)}\Psi(\theta = 0). \tag{A.7}$$

The above transformation can be broken into two singular transformation for the envelope function,

$$\Psi(r, \theta = 2\pi) = U(\phi)V_n(\theta)\Psi(r, \theta = 0), \tag{A.8}$$

where $U(\phi) = e^{-i\frac{\phi}{2}\sigma_z\tau_z}$ and $V_n(\theta) = e^{-i\frac{n\theta}{4}\tau_y\sigma_y}$. The Hamiltonian in equation (A.1) in polar cordinate (ρ, ϕ) can be written as

$$H(r, \phi) = -i\hbar v_F\Big[(\cos\phi\sigma_x + \sin\phi\sigma_y)\partial_r + (\cos\phi\sigma_y - \sin\phi\sigma_x)\frac{1}{r}\partial_\phi\Big] + \Delta\tau_z\sigma_z. \tag{A.9}$$

In the effective Hamiltonian, a magnetic flux Φ passing through origin is described by replacing momentum $\vec{p}$ by the conical omentum $\vec{p} + e\vec{A}$ with vector potential

$$\vec{A}(r, \phi) = \frac{\Phi}{2\pi}\frac{1}{\Omega_n r}(-\sin\phi, \cos\phi). \tag{A.10}$$

After performing the transformation of U, the Dirac Hamiltonian in polar coordinate reads at K and K' points

$$\tilde{H}(r, \phi) = \hbar v_F\left[\left(k_r - \frac{i}{2r}\right)\tau_z\sigma_x + \left(k_\phi + \frac{\Phi}{\Omega_n\Phi_0 r}\right)\sigma_y\right] + \Delta\tau_z\sigma_z \tag{A.11}$$

with $k_r = -i\partial_r$ and $k_\phi = -\frac{i}{r}\partial_\phi$. Now the second local transformation V_n effectively replaces ∂_θ by $(\partial_\theta - i\frac{n}{4}\sigma_y\tau_y)$ with rescaled ϕ in equation (A.11). After diagonalization, the final Hamiltonian form is given in equation (10).

References

1. M. Vozmediano, M. Katsnelson, F. Guinea, Phys. Rep. **496**, 109 (2010)
2. G.E. Volovik, The Universe in a Helium Droplet, in *International Series of Monographs on Physics* (Oxford University Press, 2003)
3. E.R. Pereira, S. Fumeron, F. Moraes, Phys. Rev. E **87**, 049904 (2013)
4. D. Sinha, Eur. Phys. J. B **88**, 83 (2015)
5. M.O. Katanaev, I.V. Volovich, Ann. Phys. **216**, 1 (1992)
6. S. Yeganeh, M.A. Ratner, E. Medina, V. Mujica, J. Chem. Phys. **131**, 014707 (2009)
7. E. Medina, L.A. González-Arraga, D. Finkelstein-Shapiro, B. Berche, V. Mujica, J. Chem. Phys. **142**, 194308 (2015)
8. D. Schmeltzer, New J. Phys. **14**, 063025 (2012)
9. M. Buongiorno Nardelli, B.I. Yakobson, J. Bernholc, Phys. Rev. B **57**, R4277 (1998)
10. A.H. Castro Neto, F. Guinea, N.M.R.. Peres, K.S. Novoselov, A.K. Geim, Rev. Mod. Phys. **81**, 109 (2009)
11. T. Ando, J. Phys. Soc. Jpn **74**, 777 (2005)
12. A. Krishnan, E. Dujardin, M.M.J. Treacy, J. Hugdahl, S. Lynum, T.W. Ebbesen, Nature **388**, 451 (1997)
13. S.N. Naess, A. Elgsaeter, G. Helgesen, K.D. Knudsen, Sci. Technol. Adv. Mater. **10**, 065002 (2009)
14. Y. Aharonov, D. Bohm, Phys. Rev. **115**, 485 (1959)
15. Y. Aharonov, A. Casher, Phys. Rev. Lett. **53**, 319 (1984)
16. E. Medina, A. López, B. Berche, Europhys. Lett. **83**, 47005 (2008)
17. E. Lipparini, *Modern Many-Particle Physics* (World Scientific, Singapore, 2008)
18. P. Recher, B. Trauzettel, A. Rycerz, Y.M. Blanter, C.W.J. Beenakker, A.F. Morpurgo, Phys. Rev. B. **76**, 235404 (2007)
19. M. Zarenia, J. Milton Pereira, A. Chaves, F.M. Peeters, G.A. Farias, Phys. Rev. B **81**, 045431 (2010)
20. M. Zarenia, J. Milton Pereira, A. Chaves, F.M. Peeters, G.A. Farias, Erratum, Phys. Rev. B **82**, 119906(E) (2010)
21. N. Bolívar, E. Medina, B. Berche, Phys. Rev. B **89**, 125413 (2014)
22. T. García, S. Rodríguez-Bolívar, N.A. Cordero, E. Romera, J. Phys: Condens. Matter **25**, 235301 (2013)
23. J. Gonzalez, F. Guinea, M.A.H. Vozmediano, Nucl. Phys. B **406**, 771 (1993)
24. P.E. Lammert, V.H. Crespi, Phys. Rev. Lett. **85**, 5190 (2000)
25. A. Cortijo, M.A.H. Vozmediano, Nucl. Phys. B **763**, 293 (2007)
26. O.V. Yazyev, S.G. Louie, Phys. Rev. B **81**, 195420 (2010)

27. E. Cockayne, G.M. Rutter, N.P. Guisinger, J.N. Crain, P.N. First, J.A. Stroscio, Phys. Rev. B. **83**, 195425 (2011)
28. B. An, S. Fukuyama, K. Yokogawaa, M. Yoshimura, M. Egashira, Y. Korai, I. Mochida, Appl. Phys. Lett. **78**, 3696 (2001)
29. A. Hashimoto, K. Suenaga, A. Gloter, K. Urita, S. Iijima, Nature **430**, 870 (2004)
30. E.J. Duplock, M. Scheffler, P.J.D. Lindan, Phys. Rev. Lett. **92**, 225502 (2004)
31. A. Ruegg, C. Lin, Phys. Rev. Lett **110**, 046401 (2013)
32. E. McCann, V.I. Fal'ko, Phys. Rev. Lett. **96**, 086805 (2006)
33. P. Recher, J. Nilsson, G. Burkard, B. Trauzettel, Phys. Rev. B **79**, 085407 (2009)
34. F. Guinea, M.I. Katsnelson, A.K. Geim, Nat. Phys. **6**, 30 (2010)
35. P. Ghaemi, J. Cayssol, D.N. Sheng, A. Viswanath, Phys. Rev. Lett. **108**, 266801 (2012)
36. A. Ruegg, C. Lin, Phys. Rev. Lett **110**, 046401 (2013)
37. L. Brey, H.A. Fertig, Phys. Rev. B **73**, 235411 (2006)
38. F.E. Meijer, A.F. Morpurgo, T.M. Klapwijk, Phys. Rev. B **66**, 033107 (2002)
39. B. Berche, C. Chatelain, E. Medina, Eur. J. Phys. **31**, 1267 (2010)
40. U.C. Coskun, T.-C. Wei, S. Vishveshwara, P.M. Goldbart, A. Bezryadin, Science **304**, 1132 (2004)
41. G. Fedorov, P. Barbara, D. Smirnov, D. Jiménez, S. Roche, Appl. Phys. Lett. **96**, 132101 (2010)
42. M. Trushin, J. Schliemann, Phys. Rev. Lett. **107**, 156801 (2011)
43. M. Mecklenburg, B.C. Regan, Phys. Rev. Lett. **106**, 116803 (2011)
44. G. Rempe, H. Walther, N. Klein, Phys. Rev. Lett. **58**, 353 (1987)
45. J.A. Yeazell, M. Mallalieu, C.R. Stroud, Jr., Phys. Rev. Lett. **64**, 2007 (1990)
46. M.J.J. Vrakking, D.M. Villeneuve, A. Stolow, Phys. Rev. A **54**, R37 (1996)
47. G. Della Valle, M. Savoini, M. Ornigotti, P. Laporta, V. Foglietti, M. Finazzi, L. Duò, S. Longh, Phys. Rev. Lett. **102**, 180402 (2009)
48. E.A. Shapiro, M. Spanner, M.Y. Ivanov, Phys. Rev. Lett. **91**, 237901 (2003)
49. M. Spanner, E.A. Shapiro, M.Y. Ivanov, Phys. Rev. Lett. **92**, 093001 (2004)
50. K.F. Lee, D.M. Villeneuve, P.B. Corkum, E.A. Shapiro, Phys. Rev. Lett. **93**, 233601 (2004)
51. M. Mehring, K. Müller, I.Sh. Averbukh, W. Merkel, W.P. Schleich, Phys. Rev. Lett. **98**, 120502 (2007)
52. M. Gilowski, T. Wendrich, T. Müller, Ch. Jentsch, W. Ertmer, E.M. Rasel, W.P. Schleich, Phys. Rev. Lett. **100**, 030201 (2008)
53. D. Bigourd, B. Chatel, W.P. Schleich, B. Girard, Phys. Rev. Lett. **100**, 030202 (2008)
54. I. Sh. Averbukh, J.F. Perelman, Phys. Lett. A **139**, 449 (1989)
55. V. Krueckl, T. Kramer, New J. Phys. **11**, 093010 (2009)
56. R.W. Robinett, Phys. Rep. **392**, 1 (2004)
57. E. Romera, F. de los Santos, Phys. Rev. B **80**, 165416 (2009)